Mass Transfer from a Contaminated Fluid Sphere

Abdellah Saboni
Laboratoire de Thermique, Energétique et Procédés, UPPA-IUT, Avenue de l'Université, 64000 Pau, France

Silvia Alexandrova
Laboratoire de Thermique, Energétique et Procédés, ENSGTI, rue Jules Ferry, BP 7511, 64 075 Pau Cedex, France

Maria Karsheva
Dept. of Chemical Engineering, University of Chemical Technology and Metallurgy, 1756 Sofia, Bulgaria

Christophe Gourdon
Laboratoire de Génie Chimique, ENSIACET BP 1301, 5, rue Paulin Talabot, 31106 Toulouse Cedex 1, France

DOI 10.1002/aic.12391
Published online August 26, 2010 in Wiley Online Library (wileyonlinelibrary.com).

The unsteady mass transfer from a contaminated fluid sphere moving in an unbounded fluid is examined numerically for unsteady-state transfer. The effect of the interface contamination and the flow regime on the concentration profiles, inside and outside a fluid sphere, is investigated for different ranges of Reynolds number ($0 <$ Re < 200) and Peclet number ($0 <$ Pe $< 10^5$), viscosity ratio between the dispersed phase and the continuous phase ($0 < \kappa < 10$), and the stagnant-cap angle ($0° < \theta_{cap} < 180°$). It was found that the stagnant-cap angle significantly influences the mass transfer from the sphere to a surrounding medium. For all Peclet and Reynolds numbers and κ, the contamination reduces the mass transfer flux. The average Sherwood number increases with an increase of stagnant-cap angle and reaches a maximum equal to the average one for a clean fluid sphere at low viscosity ratio and large Peclet numbers. A predictive equation for the Sherwood number is derived from these numerical results.
 AIChE J, 57: 1684–1692, 2011
Keywords: fluid sphere, viscosity ratio, interface contamination, mass transfer

Introduction

Knowledge of the basic phenomena occurring between a fluid sphere and an external flow is important for the understanding of transport phenomena in many liquid–liquid, solid–liquid, and gas–liquid systems in chemical and biochemical processing, environmental engineering, and minerals refining. The most significant achievements in the field are summarized in the books of Clift et al.[1] and Sadhal et al.[2] For creeping flow ($0 < Re < 1$), the solutions of the diffusion–convection equation with flow field of the Hadamard-Rybczynski or Stokes were obtained by numerical integration.[1] The numerical results show that the concentration contours are not symmetrical and that the flow inside and outside the sphere significantly influences mass transfer. In the case of a sphere with low viscosity ratio, the mass transfer is facilitated.[3] At higher Reynolds numbers, numerical solutions of the Navier Stokes and diffusion–convection equations have been obtained by different authors.[4–14] The effect of the viscosity ratio on the flow and mass transfer from a fluid sphere was studied by Clift et al.,[1] Oliver and DeWitt,[15] Feng and Michaelides,[13,16] Saboni and Alexandrova,[8] Saboni et al.,[9,13] and Kishore et al.[14]

Correspondence concerning this article should be addressed to A. Saboni at abdellah.saboni@univ-pau.fr.

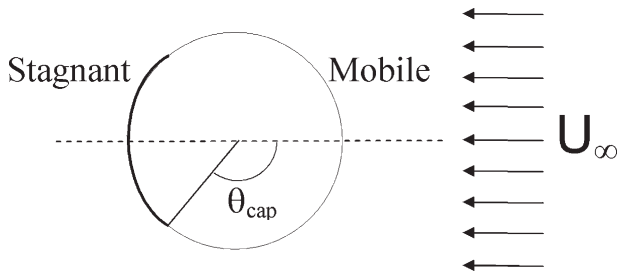

Figure 1. Stagnant-cap model.

The effects of the contamination on the mass transfer from bubbles and drops were studied for many years. The stagnant-cap model[17] is the conceptual model widely used for modeling of mass transfer from contaminated bubbles description. The model assumes that surface-active agents tend to accumulate at the rear of the bubble, forming a cap with immobile surface while the rest of the sphere surface remains mobile (Figure 1). For slightly soluble or insoluble surfactants with high Peclet numbers, the surface convection is fast when compared with surface diffusion, and surfactant is collected in a stagnant cap at the rear of the fluid sphere while the front is mobile. In this case, the stagnant-cap model is applicable. This model has been widely used to describe the flow around contaminated bubbles. The magnitude of contamination is described by the polar angle θ_{cap} of the spherical coordinate system with z-axis coinciding with the direction of the relative motion of the bubble or drop in the fluid. These model predictions are in good agreement with the experimental observations of several authors[17–23] who reported the formation of a stagnant cap at the rear of a drop or a bubble contaminated with slightly soluble surfactant (high Peclet numbers). The case of the creeping flow (Stokes flow) past bubbles with stagnant cap has also been investigated.[18,24–26] The problem was generalized by Sadhal and Johnson[27] to include both drops and bubbles. In their study, steady creeping flow past a viscous fluid sphere partially coated with thin films was examined analytically. Sadhal and Johnson[27] showed that the surfactant would collect in a cap on the bottom of the bubble and obtained an analytical solution. Bel Fdhila and Duineveld[28] have extended the approach of Sadhal and Johnson[27] to finite Reynolds numbers by solving the Navier-Stokes equations around a spherical bubble coupled with a stagnant-cap model. McLaughlin[29] analyzed the effects of an insoluble surfactant on the flow around a deforming bubble rising steadily in water. He used a modification of the procedure developed by Ryskin and Leal[30] to simulate the flow field around the deforming bubble. In that work, the computed rise velocity is in good agreement with the experimental values obtained by Duineveld.[31] Cuenot et al.[32] analyzed the effects of slightly soluble surfactants on the flow around a spherical bubble for a Reynolds number $Re = 100$. In the same work, the models of surface mobility of bubbles in surfactant solution have been reviewed. The work of Cuenot et al.[32] included the unretarded surface, uniformly retarded surface, stagnant cap, and completely stagnant surface models. Their results confirmed the validity of the stagnant-cap model for description of the flow around a bubble contaminated by slightly soluble surfactants for most practical situations. They also demonstrated that a simple relation between the cap angle and the bulk concentration cannot be generally obtained because of the significant role of the diffusion from the bulk. Takemura and Yabe[33] studied the dissolution rate of gas bubbles experimentally and numerically. They measured the bubble size and rising speed and estimated the drag coefficient and the Sherwood number. They also numerically estimated the drag coefficient, C_D, and the Sherwood number by solving the coupled Navier-Stokes and convection–diffusion equations. The comparison between the measured and the calculated rise velocities showed satisfactory agreement. Ponoth and McLaughlin[34] investigated the effect of surfactants on the dissolution rate of carbon dioxide bubble on water, calculating the velocity field around a bubble together with its shape using a boundary fitted grid and a finite difference method and by solving the unsteady convective diffusion equation for the concentration field. Liao and McLaughlin[35] reported results of numerical simulations of bubble behavior in dilute surfactant solutions. They considered the buoyancy-driven motion of a single bubble in an unbounded liquid that was at rest. They used the stream function-vorticity formulation of the Navier-Stokes equation. The governing equations were solved by a finite difference method using an adaptive boundary-fitted coordinate system. This work was revisited by Liao et al.[36] who showed that the simulations contained some inaccuracy associated with the numerical algorithm used to solve the surfactant transport equation on the bubble surface. When Liao et al.[36] corrected the problem, the simulations agreed much better with the experimental data. The effect of surfactants on mass transfer coefficient for bubbles was investigated by Vasconcelos et al.,[37] Painmanakul et al.,[38] Sardeing et al.,[39] Madhavi et al.,[40] and Maceiras et al.[41] Dani[42] studied the mass transfer between a single bubble and a liquid. The mass transfer has been investigated by solving the Navier-Stokes equation and diffusion–convection equation around a bubble for a wide range of Reynolds numbers ($0.01 \leq Re \leq 300$), Schmidt numbers ($1 \leq Sc \leq 10^5$), and bubble surface contamination degrees ($0^\circ \leq \theta_{cap} \leq 180^\circ$).

In this study, the generalized model of mass transfer from contaminated fluid spheres to continuous phase was developed, in which the viscosity ratio ($\kappa = \mu_d/\mu_c$) between the dispersed phase and the continuous phase differs from zero, contrary to a bubble for which it is not necessary to resolve the interior flow field. In the case of a fluid sphere with nonzero viscosity ratio, the situation is more complicated than that of a bubble because there is a coupling between the flow inside and outside of the fluid sphere, and by consequence, the Naviers Stokes equations inside and outside of the fluid sphere must be solved. Dispersed systems with intermediate viscosity ratio usually occur in industrial processes for instance in the liquid–liquid extraction where the viscosity ratio may vary between 0.05 and 10.

In this work, we solve the Navier-Stokes equations inside and outside a contaminated fluid sphere and the diffusion–convection equation outside the contaminated fluid sphere. This article presents the results of a parametric numerical study in which the Sherwood numbers from a spherical fluid volume were computed over the ranges $0.1 < Re < 200$, $0 < Pe < 10^5$, and $0 < \kappa < 10$ for seven different values of the polar angle θ_{cap} characterizing the extent of the rigid cap at the rear of the bubble or drop ($\theta_{cap} = 0^\circ$, 30°, 64°, 90°,

124°, 150°, and 180°). We consider Reynolds numbers not exceeding 200. This Reynolds number value is the highest limit for which the flow rests axisymmetric in the case of the rigid sphere and for which an air bubble in water remains quasi-spherical. This article is divided as follows: the governing equations and the method of solution are described in the next section, and the results of the numerical computations are given in Results and Discussion section. The results are analyzed in terms of the concentrations contours maps outside the fluid particle and in terms of variations in the average and the local Sherwood numbers.

Governing Equations

A contaminated fluid sphere of radius a and concentration C_0 is considered. It is moving with uniform velocity, U_∞, in another immiscible fluid of infinite extent volume with a different concentration denoted by C_∞. As the flow field depends on Reynolds number, the mass transfer rate will depend on both the Reynolds and the Peclet numbers. Thus, it is necessary to solve the Navier-Stokes equations to obtain the velocity field and to use it for the solution of the diffusion–convection equation. As the flow is considered axisymmetric, the Navier-Stokes equations can be written in terms of stream function and vorticity (ψ and ω) in spherical coordinates r and θ.[1,2]

$$E^2\psi_d = \omega_d r \sin\theta, \tag{1}$$

and

$$\frac{\mu_c}{\mu_d}\frac{\rho_d}{\rho_c}\frac{Re}{2}\left[\frac{\partial\psi_d}{\partial r}\frac{\partial}{\partial\theta}\left(\frac{\omega_d}{r\sin\theta}\right)-\frac{\partial\psi_d}{\partial\theta}\frac{\partial}{\partial r}\left(\frac{\omega_d}{r\sin\theta}\right)\right]\sin\theta = E^2(\omega_d r\sin\theta), \tag{2}$$

where $E^2 = \frac{\partial^2}{\partial r^2}+\frac{\sin\theta}{r^2}\frac{\partial}{\partial\theta}\left(\frac{1}{\sin\theta}\frac{\partial}{\partial\theta}\right)$.

Outside the fluid sphere, the above equations are still valid, but for numerical reasons, the radial coordinate r is transformed via $r = e^z$, where z is the logarithmic radial coordinate. The results are as follows:

$$E^2\psi_c = \omega_c e^z \sin\theta, \tag{3}$$

and

$$\frac{Re}{2}\left[\frac{\partial\psi_c}{\partial z}\frac{\partial}{\partial\theta}\left(\frac{\omega_c}{e^z\sin\theta}\right)-\frac{\partial\psi_c}{\partial\theta}\frac{\partial}{\partial z}\left(\frac{\omega_c}{e^z\sin\theta}\right)\right]e^z\sin\theta = e^{2z}E^2(\omega_c e^z\sin\theta). \tag{4}$$

All variables are normalized by introducing the following dimensionless quantities:

$$r = r'/a;\quad \omega = \omega' a/U_\infty;\quad \psi = \psi'/(U_\infty a^2);\quad Re = 2aU_\infty/\nu_c,$$

where a is the sphere radius, Re is the Reynolds number, U_∞ is the terminal velocity, and ν is the kinematic viscosity. The primes denote the dimensional quantities, and subscripts d and c refer to dispersed and continuous phase, respectively. In terms of dimensionless stream function, ψ, the dimensionless radial and tangential velocities are given by:

$$u = -\frac{1}{r^2\sin\theta}\frac{\partial\psi}{\partial\theta};\quad v = \frac{1}{r\sin\theta}\frac{\partial\psi}{\partial r}. \tag{5}$$

The boundary conditions to be satisfied are as follows:

(i) Far from the fluid sphere ($z = z_\infty$), undisturbed parallel flow is assumed: $\omega_c = 0$; $\psi_c = 0.5e^{2z}\sin^2\theta$.

(ii) Along the axis of symmetry ($\theta = 0°, \pi$): $\psi_c = 0$, $\omega_c = 0$, $\psi_d = 0$, $\omega_d = 0$.

(iii) Across the mobile part of the interface ($\theta < \theta_{cap}$ and $z = 0$ or $r = 1$), the following relations account for negligible mass transfer, continuity of tangential velocity, and continuity of tangential stress, respectively:

$$\psi_c = 0;\quad \psi_d = 0;\quad \frac{\partial\psi_c}{\partial z} = \frac{\partial\psi_d}{\partial r};\quad \frac{\mu_c}{\mu_d}\left(\frac{\partial^2\psi_c}{\partial z^2}-3\frac{\partial\psi_c}{\partial z}\right) = \left(\frac{\partial^2\psi_d}{\partial r^2}-2\frac{\partial\psi_d}{\partial r}\right),$$

where μ is the dynamic viscosity.

(iv) Across the stagnant part of the interface ($\theta > \theta_{cap}$ and $z = 0$ or $r = 1$), the tangential velocity is zero:

$$\psi_c = 0;\quad \psi_d = 0;\quad \frac{\partial\psi_c}{\partial z} = \frac{\partial\psi_d}{\partial r} = 0.$$

Equations 1–4 subjected to the boundary conditions (i) to (iv) are solved simultaneously to obtain stream function and vorticity values. Once the stream function is known, the velocities can be determined from Eq. 5.

The concentration distribution can then be calculated from the diffusion–convection equation. As the flow is considered axisymmetric, the unsteady convective mass transfer from a fluid sphere in spherical coordinates r and θ is described by the following dimensionless diffusion–convection equation:

$$\frac{\partial C}{\partial t}+\frac{Pe}{2e^z}\left(u\frac{\partial C}{\partial z}+v\frac{\partial C}{\partial\theta}\right) = \frac{1}{e^{2z}}\left(\frac{\partial^2 C}{\partial z^2}+\frac{\partial C}{\partial z}+\frac{\partial^2 C}{\partial\theta^2}+\cot(\theta)\frac{\partial C}{\partial\theta}\right), \tag{6}$$

where Pe is the Peclet number ($Pe = 2aU_\infty/D$), D is the diffusivity, t is the time ($t = Dt'/a^2$), $z = \ln(r)$, and C is the dimensionless concentration based on the initial concentration difference:

$$C = \frac{C' - C'_\infty}{C'_{d,0} - C'_\infty}.$$

The boundary and initial conditions to be satisfied are as follows:

(i) Far from the fluid sphere ($r \to \infty$): $C = 0$.

(ii) Along the axis of symmetry ($\theta = 0°$ and π): $\frac{\partial C}{\partial\theta} = 0$.

(iii) Across the interface ($r = 1$): $C = 1$.

(iv) At $t = 0$: $C(z,\theta) = 0$.

The surface and average Sherwood numbers are computed from the mass transfer flux from the surface of the sphere:

$$Sh_{surface} = -2\left(\frac{\partial C}{\partial r}\right)_{r=1}, \tag{7}$$

Table 1. Comparison of the Present Results for Sherwood Number with the Dani[42] Numerical Solution for the Case of Bubble ($\kappa = 0$) at Creeping Flow

	$\theta_{cap} = 0$		$\theta_{cap} = 90$		$\theta_{cap} = 180$	
Pe	Dani[42]	Present Results	Dani[42]	Present Results	Dani[42]	Present Results
1	2.30	2.35	2.31	2.37	2.34	2.40
10	3.25	3.26	3.38	3.40	3.68	3.71
50	4.70	5.18	5.18	5.52	6.24	6.34
100	–	5.65	6.45	6.50	8.17	8.18
500	8.88	8.99	11.50	11.65	16.41	16.40
1000	10.92	11.05	15.10	15.33	22.73	22.52

$$Sh = -\int_0^{\pi} \left(\frac{\partial C}{\partial r}\right)_{r=1} \sin\theta \, d\theta. \tag{8}$$

Equations 1–6 together with the above boundary conditions are evaluated numerically with several combinations of parameters. The equations of motion inside and outside the fluid sphere are solved by finite difference approximations. The elliptic stream function equations are solved iteratively, and the parabolic vorticity equations are solved by means of the alternating direction implicit method. Once the stream function is known, the velocities are then determined from Eq. 5. To discretize the time-dependant diffusion–convection equation (Eq. 6), the forward-central (forward in time and central differencing in space) explicit scheme is used. It is desirable to have a finer mesh near the sphere where the gradients are large. For this the $r = \exp(z)$ transformation is used. Then the grid in the continuous phase is generated with uniform spacing in z and θ. Only half of the physical domain was used because the line $\theta = 0°$ and π is a line of symmetry. To obtain precise results with minimal computing time, the selection of the grid was obtained using data from previous studies (rigid sphere and bubble) and by making tests with different mesh sizes. For $Pe < 5000$, a computational grid number in radial and tangential direction are 401×91, respectively. For instance for $Pe = 50{,}000$, a computational grid number in radial and tangential direction are 1201×91, respectively. In addition, the distance from the sphere to the edge of the computational domain is 200 diameters for low Peclet numbers ($Pe \sim 1$) and 12 diameters for higher Peclet numbers ($Pe > 10$) for which the boundary layer thickness is less. The validation of the numerical methods used implied two stages: (1) the checking of the numerical solution procedure concerning the hydrodynamics around and inside a fluid sphere, and (2) the checking of the numerical method used for the mass transfer. Detailed discussions on the accuracy of the solution procedure used for the momentum, continuity equations, and diffusion–convection equation for the case of uncontaminated fluid sphere were previously made by Saboni and Alexandrova[9] and Saboni et al.[13] They used a computer code based on the same principles and investigated the effects of the viscosity ratio and the flow on the concentration profiles for Reynolds number, viscosity ratio, and Peclet number ranges of $0 \le Re \le 400$, $0 \le \kappa \le 1000$, and $0 \le Pe \le 1{,}000{,}000$, respectively. The validation of the numerical procedure used here was focused on the effect of the contamination. To validate the mathematical procedure for the contaminated fluid sphere ($0 < \kappa < 10$), our numerical simulation was run at low Reynolds numbers ($Re \to 0$) —creeping flow, as well as at higher Reynolds number ($Re = 100$) for comparison with the available literature results for a contaminated bubble ($\kappa = 0$).

Results and Discussion

First, the solution method was tested for the limiting case of a bubble ($\kappa = 0$). The numerical results for the Sherwood number at creeping flow ($Re \to 0$) are compared in Table 1 with the numerical solution given by Dani.[42] For different stagnant-cap angles ($\theta_{cap} = 180°$, 90°, and 0°), it shows a good agreement between our results and those of Dani.[42] For the case of bubble ($\kappa = 0$) at higher Reynolds numbers, the Sherwood numbers computed by our numerical model are compared in Table 2 with the results of Takemura and Yabe[33] and Dani.[42] A good agreement is found for both Reynolds numbers considered ($Re = 10$ and $Re = 100$), Peclet numbers ($Pe = 5000$, 50,000), and the different stagnant-cap angles ($\theta_{cap} = 180°$, 124°, 90°, 64°, and 0°).

Another set of numerical experiments considered for the case of the mass transfer from fluid sphere with κ ($\kappa = \mu_d/\mu_c$) different from zero contrary to a bubble. Figure 2 shows streamline contours inside and outside a fluid sphere for $Re = 50$, $\kappa = 1$, and different stagnant-cap angles. At high stagnant-cap angles ($\theta_{cap} = 180°$ and 124°), it appears that internal circulation is sufficiently rapid to prevent flow separation and the formation of a trailing vortexes. Slight asymmetry is observed between upstream and downstream regions near the sphere. For the low stagnant-cap angles, the contour line plots show flow separation downstream the fluid particle, which is very similar in all cases with $0° < \theta_{cap} < 90°$. The effect of the angle θ_{cap} characterizing the degree of contamination is mainly concerned with the flow inside the fluid

Table 2. Comparison of the Present Results for Sherwood Number with Other Numerical Studies for the Case of Bubble ($\kappa = 0$)

	θ_{cap}				
	0	64	90	124	180
$Re = 10$, $Sc = 500$					
Takemura and Yabe[33]	20	30	40	51	56
Dani[42]	21	29	40	53	58
Present results	21	30	42	55	60
$Re = 100$, $Sc = 500$					
Takemura and Yabe[33]	58	110	155	197	214
Dani[42]	60	116	164	205	218
Present results	60	108	163	206	220

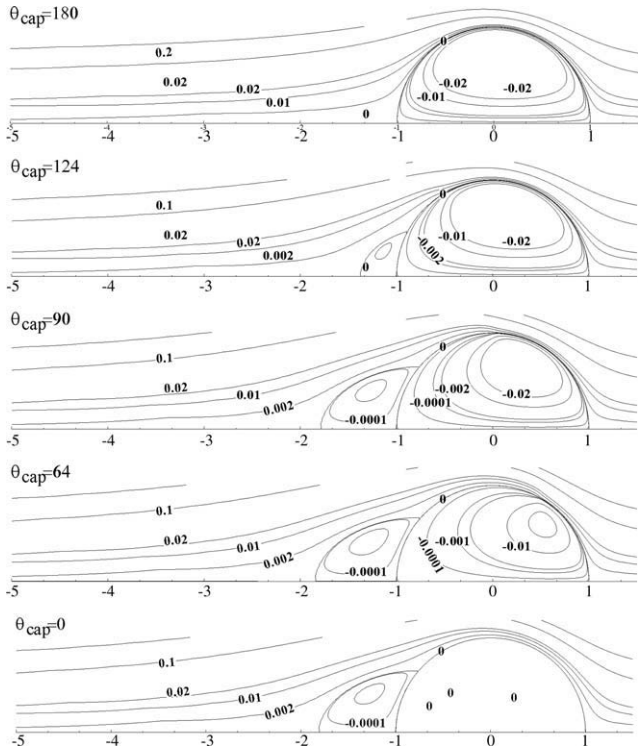

Figure 2. Stream function contours, inside and outside a fluid sphere for Re = 50, κ = 1, and different stagnant caps.

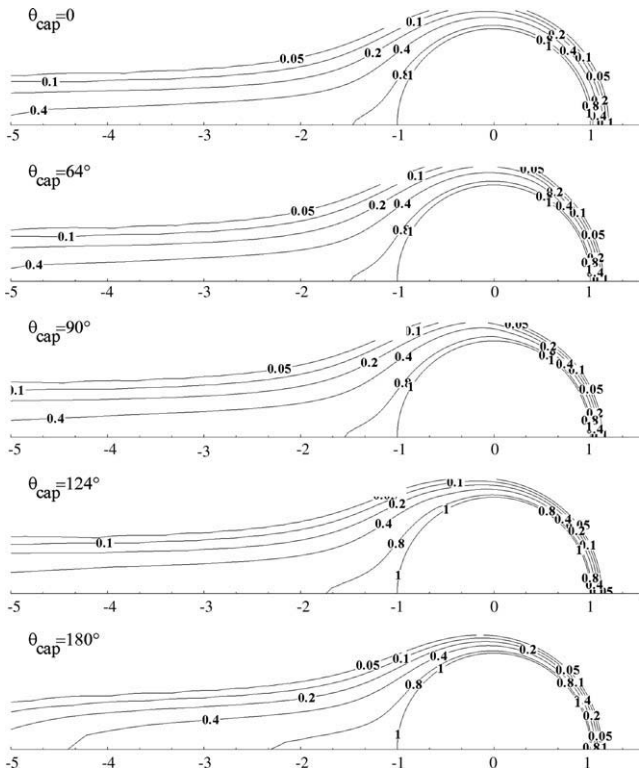

Figure 3. Concentration contour lines around a fluid sphere for Re = 0.1, Pe = 1000, and κ = 1.

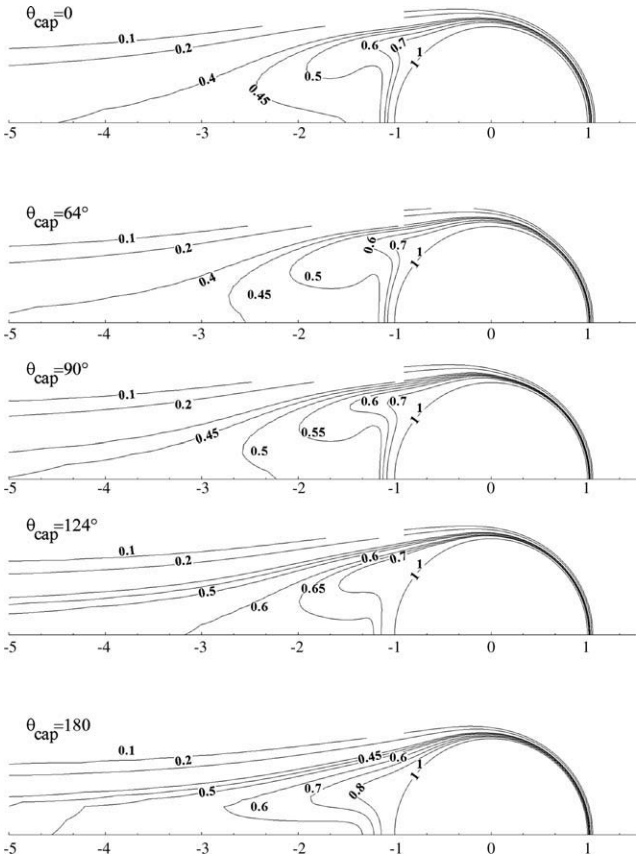

Figure 4. Concentration contour lines around a fluid sphere for Re = 100, Pe = 1000, and κ = 3.

particle, which has a limited effect on the drag coefficient. Similar conclusions are derived for other Reynolds numbers $Re < 200$ (data not shown here).

Figure 3 shows the concentration profiles around clean fluid spheres ($\theta_{cap} = 180°$), around partially contaminated spheres ($\theta_{cap} = 124°$, 90°, and 64°), and around fully contaminated fluid spheres ($\theta_{cap} = 0°$) at creeping flow for a fixed viscosity ratio $\kappa = 1$. The incident stream conveys the front layers to the rear of the sphere so that the extension of the concentration boundary layer with the fluid is deeper at the rear than at the front. This phenomenon leads to changes in concentrations field—an elongation of concentration contour lines in the flow direction. It is evident that the domain of high concentrations in the downstream region of the sphere is larger in the case of a noncontaminated fluid sphere than that in the case of a partially or totally contaminated sphere. This can be explained with a higher mass transfer rate for the noncontaminated fluid sphere in comparison with a partially or totally contaminated one. On the mobile part of the interface, the mass transfer is facilitated as a result of convection and diffusion. On the other hand, on the immobile part of the interface, the mass transfer is due to diffusion only.

Figure 4 shows the concentration around clean fluid spheres ($\theta_{cap} = 180°$), around partially contaminated spheres ($\theta_{cap} = 124°$, 90°, and 64°), and around fully contaminated fluid spheres ($\theta_{cap} = 0°$) at $Re = 100$, $Pe = 1000$, and $\kappa = 3$. Similar to Figure 3, the same general observation concerning the front layer can be made. In addition, the concentration

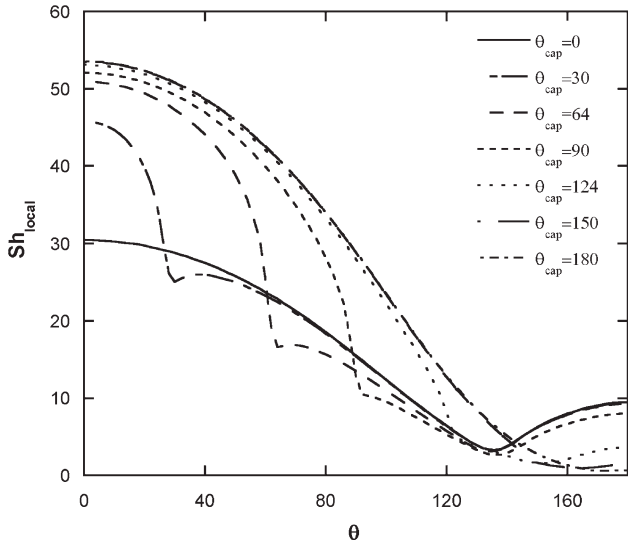

Figure 5. Local Sherwood number along the drop surface for Re = 100, κ = 1, and Pe = 1000.

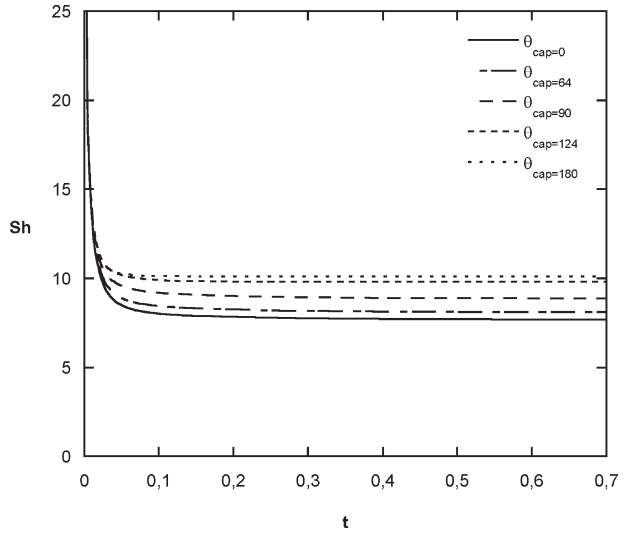

Figure 7. Variation of Sherwood number with dimensionless time for Re = 100, κ = 1, and Pe = 100.

wake is larger, which indicates that the convection is increased due to the increased Reynolds number. The important effect of the hydrodynamics on the mass transfer must be underlined. As a result, concentration contour lines at highly contaminated case ($\theta_{cap} = 0°$) tend to follow the streamlines in the wake region because of the presence of a strong recirculation flow in this region.

For the steady state, local distributions for $Re = 100$, different stagnant-cap angles ($\theta_{cap} = 0°$, 30°, 64°, 90°, 124°, 150°, and 180°), and a viscosity ratio $\kappa = 1$ are presented in Figure 5 indicating the effect of the contamination on the mass transfer. As the stagnant-cap angle increases, the concentration boundary layer becomes thinner, and thus leading to higher mass transfer rates. In all cases, the maximum value for the Sherwood number occurs at the front stagnation. Thus, the local Sherwood numbers decrease with the increase of the angular position until a minimum value is reached. For lower stagnant-cap angles ($\theta_{cap} = 0°$, 30°, 64°, and 90°), the Sherwood number increases with further increase of the angular position because of the flow separation after the location of the minimum value of the Sherwood number, whereas for higher stagnant-cap angles ($\theta_{cap} = 124°$, 150°, and 180°), the minimum value occurs in the vicinity of the rear stagnation point. For low contamination ($\theta_{cap} \sim 150°$), the local Sherwood number value is rather close to the local Sherwood number of a clean fluid sphere ($\theta_{cap} = 180°$). For higher contamination, two parts in the profile of the local Sherwood number are observed, separated by θ_{cap}. For the contaminated part of the fluid sphere ($\theta > \theta_{cap}$), the local Sherwood number is lower than that of a fluid sphere and closer to that of a completely contaminated fluid sphere ($\theta_{cap} = 0°$) as the contamination increases. On the clean part of the fluid sphere ($\theta < \theta_{cap}$), the local

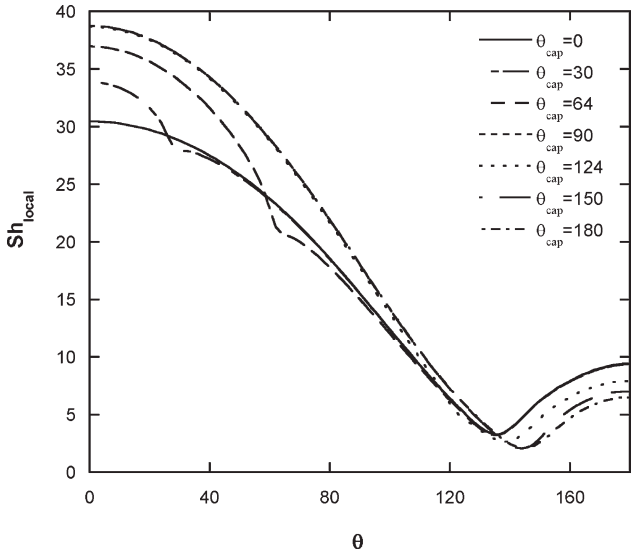

Figure 6. Local Sherwood number along the drop surface for Re = 100, κ = 10, and Pe = 1000.

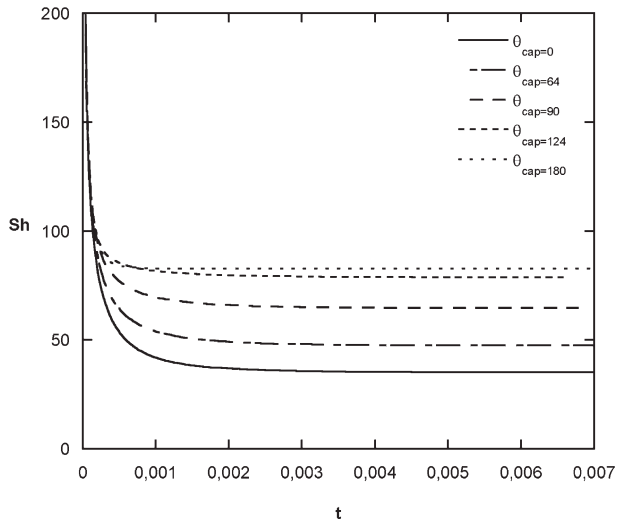

Figure 8. Variation of Sherwood number with dimensionless time for Re = 100, κ = 1, and Pe = 10,000.

Table 3. Effect of the Interface Contamination on Sherwood Number for Creeping Flow

		θ_{cap}						
κ	Pe	0	30	64	90	124	150	180
0	1	2.35	2.35	2.36	2.37	2.39	2.39	2.40
	10	3.26	3.27	3.30	3.40	3.59	3.69	3.71
	100	5.65	5.67	5.92	6.50	7.52	8.05	8.18
	1000	11.05	11.13	12.50	15.33	19.85	22.01	22.54
1	1	2.35	2.36	2.36	2.36	2.37	2.37	2.38
	10	3.26	3.27	3.29	3.34	3.43	3.47	3.48
	100	5.65	5.66	5.80	6.11	6.62	6.87	6.93
	1000	11.05	11.10	11.90	13.47	15.93	17.05	17.32
3	1	2.35	2.35	2.35	2.36	2.36	2.36	2.37
	10	3.26	3.26	3.28	3.30	3.35	3.36	3.37
	100	5.65	5.66	5.73	5.89	6.14	6.26	6.28
	1000	11.05	11.08	11.51	12.33	13.60	14.18	14.31
10	1	2.35	2.35	2.36	2.36	2.36	2.36	2.36
	10	3.26	3.26	3.27	3.28	3.29	3.30	3.30
	100	5.65	5.65	5.68	5.74	5.83	5.87	5.87
	1000	11.05	11.06	11.22	11.52	11.98	12.20	12.23

Sherwood strongly decreases with the contamination. This is due to the slowing down of the flow on the fluid sphere surface because of the immobilized part that is downstream. It is evident that the contamination leads to the mass transfer decrease both in the contaminated part and in the uncontaminated part.

Figure 6 shows steady-state local distributions of the Sherwood number for $Re = 100$, different stagnant-cap angles ($\theta_{cap} = 0°$, 30°, 64°, 90°, 124°, 150°, and 180°), $Pe = 1000$, and viscosity ratio of $\kappa = 10$. Here also, with the increase of the stagnant-cap angle, the concentration boundary layer becomes thinner, and thus increasing the mass transfer rates. In all cases, the maximum value for the Sherwood number occurs at the front stagnation. Thus, the local Sherwood number decreases with the increase of the angular position until reaching the minimum value. For all stagnant-cap angles ($\theta_{cap} = 0°$, 30°, 64°, 90°, 124°, 150°, and 180°), the Sherwood number increases with further increase of the angular position due to the flow separation after the location of the minimum value of the Sherwood number.

Figures 7 and 8 show the time history of the average Sherwood number for two different Peclet numbers ($Pe = 100$ and $Pe = 10{,}000$) and different stagnant-cap angles ($0° \leq \theta_{cap} \leq 180°$). The figures show that, initially, the Sherwood number is quite high and diffusion dominates as the mass transfer mode. The Sherwood number decreases with time and approaches an asymptotic value depending on the predominance of the convective transfer. It can also be seen that the instantaneous and the asymptotic mean Sherwood number increases with the stagnant-cap angle increase.

The calculated steady-state values of average Sherwood numbers for creeping flow, $Re = 10$, 100, and 200, different Peclet numbers ($1 < Pe < 10^5$), different stagnant-cap angles ($\theta_{cap} = 180°$, 124°, 90°, 64°, and 0°), and viscosity ratios ($\kappa = 0$, 1, 3, and 10) are presented in Tables 3–6. From Table 3, it is evident that the contamination reduces the mass transfer between the fluid sphere and the continuous environment for all Peclet numbers and the viscosity ratios. It can be seen that the average Sherwood number increases with a stagnant-cap angle increase and reaches a limit value corresponding to the average Sherwood number for a clean fluid sphere. We also notice that for low viscosity ratio and large Peclet numbers, the effect is much more pronounced. For $\kappa = 0$ and $Pe = 1$, the ratio between the Sherwood of the noncontaminated fluid sphere and that of the contaminated sphere is in the order of 1, whereas for $Pe = 1000$ and $\kappa = 0$, it is in the order of 2. For $\kappa = 10$ and $Pe = 1$, the ratio is always in the order of 1, whereas for $\kappa = 10$ and $Pe = 1000$, the ratio is in the order of 1.1.

For higher Reynolds numbers, the effect of the contamination on the mass transfer is even more spectacular and here also the most important differences correspond to the low viscosity ratios and large Peclet numbers. This is illustrated in Tables 5 and 6. Table 5 shows that for $Re = 100$, $\kappa = 0$, and $Pe = 10$, the ratio between the Sherwood of the uncontaminated fluid sphere and that of the contaminated one is 1.12, whereas for $\kappa = 0$ and $Pe = 50{,}000$, the ratio is 3.65. For $\kappa = 10$ and $Pe = 10$, the ratio is in the order of 1.025, whereas for $\kappa = 10$ and $Pe = 50{,}000$, the ratio is 1.56. This can be explained by the fact that the contamination of the interface modifies the convection around the fluid sphere. Its contribution to the transfer is more important for higher Re and Pe values. On the other hand, for fixed Reynolds and Peclet numbers, the deviations between tangential velocities of a contaminated and an uncontaminated sphere are more

Table 4. Effect of the Interface Contamination on Sherwood Number for $Re = 10$

		θ_{cap}						
κ	Pe	0	30	64	90	124	150	180
1	10	3.63	3.62	3.65	3.73	3.83	3.86	3.87
	100	6.55	6.53	6.78	7.31	7.93	8.18	8.23
	1000	12.92	12.93	14.31	16.96	19.95	21.13	21.37
	50,000	45.34	46.26	63.72	93.59	122.84	133.17	135.05
	100,000	56.79	58.32	85.16	129.60	172.38	187.29	189.96

Table 5. Effect of the Interface Contamination on Sherwood Number for $Re = 100$

		θ_{cap}						
κ	Pe	0	30	64	90	124	150	180
0	10	3.95	3.95	4.01	4.16	4.35	4.41	4.42
	100	7.70	7.74	8.34	9.48	10.72	11.12	11.18
	1000	15.82	16.14	19.83	25.41	30.70	32.41	32.64
	50,000	60.21	64.65	108.20	163.63	206.66	218.68	220.29
	100,000	75.92	82.43	147.26	227.62	289.84	307.16	309.43
1	10	3.95	3.95	3.98	4.09	4.22	4.27	4.27
	100	7.70	7.71	8.09	8.88	9.78	10.07	10.10
	1000	15.82	15.93	18.29	22.31	26.32	27.61	27.77
	50,000	60.21	63.38	97.12	142.89	179.43	188.16	188.97
	100,000	75.92	79.87	126.13	190.12	240.48	252.52	253.85
3	10	3.95	3.95	3.97	4.03	4.11	4.13	4.13
	100	7.70	7.71	7.93	8.40	8.92	9.06	9.07
	1000	15.82	15.89	17.25	19.80	22.21	22.83	22.87
	50,000	60.21	61.56	80.85	111.34	135.32	139.43	139.43
	100,000	75.92	78.05	107.64	153.41	188.58	194.76	194.76
10	10	3.95	3.95	3.96	3.99	4.02	4.02	4.02
	100	7.70	7.70	7.79	7.98	8.18	8.22	8.22
	1000	15.82	15.86	16.36	17.39	18.37	18.55	18.55
	50,000	60.21	60.71	68.65	82.91	95.01	95.80	95.80
	100,000	75.92	76.71	89.30	111.32	129.65	131.12	131.12

important for the low viscosity ratio than for the higher one, and by consequence, higher ratio between the Sherwood numbers of the uncontaminated and of the contaminated sphere. Similar conclusions are derived for Reynolds number $Re = 200$ (Table 6).

To present the numerical results in a more convenient form to use, we tried to correlate our numerical results by an equation which would be valid for both the low and high Peclet numbers, despite the stagnant-cap angle value. The equation obtained is as follows:

$$Sh = \frac{3}{3+\kappa}\left\{\begin{array}{l}\left(1.65 + 0.67\left(\sqrt{Pe} + \frac{0.67Re}{Re+15}\left(\sqrt{Pe} - 1\right)\right)\right)0.01\theta_{cap} \\ +\frac{1}{3}\left((3+\kappa)\left(1 - 0.01\theta_{cap}\right) + \kappa 0.01\theta_{cap}\right)\left(1 - 0.12Re^{\frac{1}{3}} + (1+Pe)^{\frac{1}{3}}\left(1 + 0.12Re^{\frac{1}{3}}\right)\right)\end{array}\right\}. \quad (9)$$

The Sherwood number values derived by this formula coincide with those calculated numerically with an error less than 7% for fluid spheres with $10 < Re < 200$, $0 < \kappa < 10$, $0 < Pe < 10^5$, and $0 < \theta_{cap} < 180°$).

Conclusion

A numerical study has been carried out to investigate the effects of contamination on mass transfer from a contaminated fluid spheres with viscosity ratio between the dispersed phase and the continuous phase ($\kappa = \mu_d/\mu_c$) not necessarily equal to zero, contrary to a bubble case. This article presents the results of a parametric numerical study in which the mass transfer from a spherical fluid volume was computed over the ranges $0.1 < Re < 200$ and $0 < \kappa < 10$ ($1 < Pe < 10^5$) for seven different values of the polar angle θ_{cap} characterizing the extent of a rigid cap at the rear of the bubble or drop ($\theta_{cap} = 0°$, 30°, 64°, 90°, 124°, 150°, and 180°). The results show a strong dependence of mass transfer on the Reynolds and Peclet numbers, the viscosity ratio between the dispersed phase and the continuous phase, and the stagnant-cap angle. The stagnant-cap angle significantly influences the mass transfer from the fluid sphere to a surrounding fluid for all Peclet numbers. The steady-state results also show that the average Sherwood number value increases as Peclet number increases for a fixed stagnant-cap angle. For a fixed Peclet number, the average Sherwood number increases with the stagnant-cap angle increase and reaches a limit value corresponding to the average Sherwood number for a clean fluid sphere. An equation was derived to present the numerical results in an easier-to-use form, correlating our numerical results. The values of the

Table 6. Effect of the Interface Contamination on Sherwood Number for $Re = 200$

		θ_{cap}						
κ	Pe	0	30	64	90	124	150	180
1	10	4.01	4.01	4.04	4.15	4.31	4.36	4.37
	100	8.18	8.20	8.57	9.36	10.32	10.65	10.69
	1000	17.27	17.46	19.93	24.06	28.31	29.78	29.95
	50,000	67.01	70.88	107.61	155.78	195.38	205.00	205.88
	100,000	84.48	89.23	139.45	206.37	260.88	274.03	275.49

Sherwood number given by this formula coincide with those calculated numerically with an error less than 7% for fluid spheres with $10 < Re < 200$, $0 < \kappa < 10$, $0 < Pe < 10^5$, and $0^\circ < \theta_{cap} < 180^\circ$.

Literature Cited

1. Clift R, Grace JR, Weber ME. *Bubbles, Drops and Particles*. New York: Academic Press, 1978.
2. Sadhal SS, Ayyaswamy PS, Chung JNC. *Transport Phenomena with Drops and Bubbles*. Berlin: Springer, 1996.
3. Feng ZG, Michaelides EE. A numerical study on the transient heat transfer from a sphere at high Reynolds and Peclet numbers. *Int J Heat Mass Transfer*. 2000;43:219–229.
4. Juncu G. Unsteady heat and/or mass transfer from a fluid sphere in creeping flow. *Int J Heat Mass Transfer*. 2001;44:2239–2246.
5. Feng ZG, Michaelides EE. Heat and mass transfer coefficients of viscous spheres. *Int J Heat Mass Transfer*. 2001;44:4445–4454.
6. Chen WH. Dynamics of sulfur dioxide absorption in a raindrop falling at terminal velocity. *Atmos Environ*. 2001;35:4777–4790.
7. Juncu G. A numerical study of steady viscous flow past a fluid sphere. *Int J Heat Fluid Flow*. 1999;20:414–421.
8. Saboni A, Alexandrova S. Numerical study of the drag on a fluid sphere. *AIChE J*. 2002;48:2992–2994.
9. Saboni A, Alexandrova S, Gourdon C. Détermination de la traînée engendrée par une sphère fluide en translation. *Chem Eng J*. 2004; 98:175–182.
10. Chen WH. Air pollutant absorption by single moving droplets with drag force at moderate Reynolds numbers. *Chem Eng Sci*. 2006; 61:449–458.
11. Chhabra RP. *Bubbles, Drops and Particles in Non-Newtonian Fluids*, *2nd ed*. Boca Raton: CRC Press, 2006.
12. Kishore N, Chhabra RP, Eswaran V. Mass transfer from a single fluid sphere to power-law liquids at moderate Reynolds numbers. *Chem Eng Sci*. 2007;62:6040–6053.
13. Saboni A, Alexandrova S, Spasic AM, Gourdon C. Effect of the viscosity ratio on the mass transfer from a fluid sphere at low to very high Peclet numbers. *Chem Eng Sci*. 2007;62:4742–4750.
14. Kishore N, Chhabra RP, Eswaran V. Drag on ensembles of fluid spheres translating in a power-law liquid at moderate Reynolds numbers. *Chem Eng J*. 2008;139:224–235.
15. Oliver DLR, DeWitt KJ. Mass transfer from fluid spheres at moderate Reynolds numbers: a boundary layer analysis. Presented at the AIAA 30th Aerospace Sciences Meeting, Reno, Nevada, 1992.
16. Feng ZG, Michaelides EE. Mass and heat transfer from fluid spheres at low Reynolds numbers. *Powder Technol*. 2000;112:63–69.
17. Griffith RM. The effect of surfactants on the terminal velocity of drops & bubbles. *Chem Eng Sci*. 1962;17:1057–1070.
18. Savic P. Circulation and distortion of liquid previous drops falling through a viscous medium, Technical Report No. MT-22. Ontario, Canada: Division of Mechanical Engineering, National Research Council of Canada, 1953.
19. Garner FH, Skelland AHP. Some factors affecting droplet behaviour in liquid–liquid systems. *Chem Eng Sci*. 1955;4:149–158.
20. Elzinga ER Jr, Banchero JT. Some observations on the mechanics of drops in liquid–liquid systems. *AIChE J*. 1961;7:394–399.
21. Horton J, Fritsch TR, Kintner RC. Experimental determination of circulation velocities inside drops. *Can J Chem Eng*. 1965;43: 143–146.
22. Huang WS, Kintner RC. Effects of surfactants on mass transfer inside drops. *AIChE J*. 1969;15:735–744.
23. Beitel A, Heideger WJ. Surfactant effects on mass transfer from drops subject to interfacial instability. *Chem Eng Sci*. 1971;26: 711–717.
24. Davis RE, Acrivos A. The influence of surfactants on the creeping motion of bubbles. *Chem Eng Sci*. 1966;21:681–685.
25. Harper JF. On bubbles with small immobile adsorbed films rising in liquids at low Reynolds numbers. *J Fluid Mech*. 1973;58:539–545.
26. Harper JF. Surface activity and bubble motion. *Appl Sci Res*. 1982; 38:343–352.
27. Sadhal SS, Johnson RE. Stokes flow past bubbles and drops partially coated with thin films, Part 1: Stagnant-cap of surfactant film-exact solution. *J Fluid Dyn*. 1983;126:237–250.
28. Bel Fdhila R, Duineveld PC. The effect of surfactant on the rise of a spherical bubble at high Reynolds and Peclet numbers. *Phys Fluids*. 1996;8:310–321.
29. McLaughlin JB. Numerical simulation of bubble motion in water. *J Colloid Interface Sci*. 1996;184:614–625.
30. Ryskin G, Leal LG. Numerical solution of free-boundary problems in fluid mechanics, Part 2: Buoyancy-driven motion of a gas bubble through a quiescent liquid. *J Fluid Mech*. 1984;148:19–35.
31. Duineveld PC. The rise velocity and shape of bubbles in pure water at high Reynolds number. *J Fluid Mech*. 1995;292:325–332.
32. Cuenot B, Magnaudet J, Spennato B. The effects of slightly soluble surfactant on the flow around a spherical bubble. *J Fluid Mech*. 1997;339:25–53.
33. Takemura F, Yabe A. Rising speed and dissolution rate of a carbon dioxide bubble in slightly contaminated bubble. *J Fluid Mech*. 1999;378:319–334.
34. Ponoth SS, McLaughlin JB. Numerical simulation of mass transfer for bubbles in water. *Chem Eng Sci*. 2000;55:1237–1255.
35. Liao Y, McLaughlin JB. Dissolution of a freely rising bubble in aqueous surfactant solutions. *Chem Eng Sci*. 2000;55:5831–5850.
36. Liao Y, Wang J, Nunge RJ, McLaughlin JB. Comments on "Bubble motion in aqueous surfactant solutions". *J Colloid Interface Sci*. 2004;272:498–501.
37. Vasconcelos JMT, Orvalho SCP, Alves SS. Gas-liquid mass transfer to single previous term bubbles: next term effect of surface contamination. *AIChE J*. 2002;48:1145–1154.
38. Painmanakul P, Loubière K, Hébrard G, Mietton-Peuchot M, Roustan M. Effects of surfactants on liquid-side mass transfer coefficients. *Chem Eng Sci*. 2005;60:6480–6491.
39. Sardeing R, Painmanakul P, Hebrard G. Effect of surfactants on liquid-side mass transfer coefficients in gas-liquid systems: a first step to modeling. *Chem Eng Sci*. 2006;61:6249–6260.
40. Madhavi T, Golder AK, Samanta AN, Ray S. Studies on bubble dynamics with mass transfer. *Chem Eng J*. 2007;128:95–104.
41. Maceiras R, Alves SS, Cancela MA, Alvarez E. Effect of bubble contamination on gas-liquid mass transfer coefficient on CO_2 absorption in amine solutions. *Chem Eng J*. 2008;137:422–427.
42. Dani A. Transfert de masse entre une bulle et un liquide: simulations numériques directes et fluorescence induite par nappe laser. Thèse de doctorat de l'INSA de Toulouse, 2007.

Manuscript received Dec. 24, 2009, and revision received July 11, 2010.